Time-Resolved Mass Sensing of a Molecular Adsorbate Nonuniformly Distributed Along a Nanomechnical String

T. S. Biswas,[1] Jin Xu,[1] N. Miriyala,[2] C. Doolin,[1] T. Thundat,[2] J. P. Davis,[1,*] and K. S. D. Beach[3,†]

[1]*Department of Physics, University of Alberta, Edmonton, Alberta, Canada T6G 2E1*
[2]*Department of Chemical Engineering, University of Alberta, Edmonton, Alberta, Canada T6G 2E1*
[3]*Department of Physics and Astronomy, The University of Mississippi, University, Mississippi 38677, USA*

(Received 17 January 2015; revised manuscript received 27 April 2015; published 3 June 2015)

We show that the particular distribution of mass deposited on the surface of a nanomechanical resonator can be estimated by tracking the evolution of the device's resonance frequencies during the process of desorption. The technique, which relies on analytical models we have developed for the multimodal response of the system, enables mass sensing at much higher levels of accuracy than is typically achieved with a single frequency-shift measurement and no rigorous knowledge of the mass profile. We report on a series of demonstration experiments, in which the explosive molecule 1,3,5-trinitroperhydro-1,3,5-triazine (RDX) is vapor deposited along the length of a silicon nitride nanostring to create a dense, random covering of RDX crystallites on the surface. In some cases, the deposition is biased to produce distributions with a slight excess or deficit of mass at the string midpoint. The added mass is then allowed to sublimate away under vacuum conditions, with the device returning to its original state over about 4 h (and the resonance frequencies, measured via optical interferometry, relaxing back to their pre-mass-deposition values). Our claim is that the detailed time trace of observed frequency shifts is rich in information—not only about the *quantity* of RDX initially deposited but also about its *spatial arrangement* along the nanostring. The data also reveal that sublimation in this case follows a nontrivial rate law, consistent with mass loss occurring at the exposed surface area of the RDX crystallites.

DOI: 10.1103/PhysRevApplied.3.064002

I. INTRODUCTION

Nanoscale mechanical resonators have proven to be useful tools for chemical detection [1–3], thanks to their incredibly high sensitivity to added mass [4–7] and the ease with which their vibrational frequencies can be measured to great accuracy. For a device of tens or hundreds of picograms, molecules adsorbed onto the surface at the scale of femtograms or smaller are detectable as shifts in the resonance frequencies [8–10]. A serious limitation, however, is that the linear relationship between the amount of mass added and the change in the observed resonances involves a sometimes difficult-to-determine constant of proportionality. This fact, which goes unacknowledged in much of the literature, is a major impediment to high-accuracy nanomechanical mass sensing.

For a perfectly uniform distribution of added mass, the constant of proportionality is straightforward to compute: it is a simple geometric factor, given by the ratio of the resonator's mode-specific "effective mass" to its true inertial mass [11]. Even if the deposition is nonuniform, the situation is still manageable so long as the mass distribution is well characterized (and not too concentrated near the nodes of the detection mode). More typical of a sensing application, though, is that the distribution is of arbitrary form and more or less unknown. In that case, there is no reliable way to extract the total adsorbed mass from frequency-shift measurements [12], except at the level of an order-of-magnitude estimate.

To avoid this problem, efforts have been made to concentrate mass adsorption to specific sites on a device through complex fabrication [13]. An alternative approach has been to employ multimode measurements [14–20], which can provide some degree of spatial resolution (limited by the propagation of experimental uncertainties through the "inversion kernel" [21]). The simplest example is that both the size and location of a *point mass*—situated along a resonator with extent primarily in one dimension—can be determined from a simultaneous measurement of two resonance frequency shifts [22–25]. In a slightly different context, multimode measurements have been shown to provide single-resonator discrimination for the mass added along an array of strongly coupled devices [26].

The work reported in this paper also takes advantage of a multimode framework (described in Sec. III), and we find that silicon nitride nanostrings [27,28] are an excellent platform for our technique. Indeed, although the original experiment by Dohn and collaborators to determine the mass and location of a pointlike object was performed on cantilevers [22], it was soon recognized that the sinusoidal mode shapes characteristic of nanomechanical strings

*jdavis@ualberta.ca
†kbeach@olemiss.edu

greatly simplify the analysis [23]. As an added benefit, for materials such as stoichiometric silicon nitride, the high internal tension that draws a doubly clamped beam taut enough to become stringlike leads to correspondingly high mechanical quality factors. These high values aid in detection [29–31] and are maintained even in the presence of a metallic overlayer added to the device for the purpose of functionalization [32,33].

In a previous study on nanostrings, real-time mass sensing was mimicked by carrying out sequential frequency-shift measurements of the first two harmonics in conjunction with pick-and-place deposition of a single microparticle [23]. In our work, genuine real-time observations are made: we measure the first, third, and fifth harmonics simultaneously as a function of time while mass sublimates from the device surface. This is possible because we are able to resolve all three of these modes using optical interferometry at the midpoint of the string with the device entirely under thermomechanical actuation.

We show that measurements of any pair of modes reveal not only the instantaneous total mass of molecules adsorbed but also their distribution—at least in the regime where the distribution is smooth, slowly varying, and roughly symmetric about the resonator midpoint. We provide explicit formulas (derived in Sec. III and presented in Table II) for the mass coefficients of the uniform and nonuniform components of the adsorbate distribution in terms of all combinations of the frequency shifts measured in modes 1, 3, and 5—including the pseudoinverse result in which three measurements determine the two coefficients in the least squares sense—and we show that the variance among these estimates can be used as an effective tool to judge the combined uncertainty due to measurement error and analytical assumptions.

The multimode measurement technique also tells us about the desorption characteristics of the added molecule, here the explosive 1,3,5-trinitroperhydro-1,3,5-triazine (RDX). In particular, our analytical model is able to discriminate between two situations: (i) where RDX molecules are bound to the resonator surface and thus display first-order or Langmuir-like rate kinetics; and (ii) where the RDX molecules are bound to each other in crystalline formations (born from randomly distributed nucleation sites), and sublimation occurs primarily from the crystal interface. As we discuss in Sec. IV, our frequency-shift data support the latter interpretation. This is in keeping with our expectations, since atomic force microscopy studies have already established that RDX forms nanoscale crystallites on the silicon nitride surface (see the lower panel of Fig. 1 in Ref. [34]).

Our combined experimental and theoretical study of mass distribution and sublimation may be useful not only in the design of future explosive sensors [35,36] but also in a wide range of nanomechanical mass-sensing applications where accurate determination of adsorbed molecular mass is relevant. We expect it to have particular importance for single-molecule mass spectroscopy [12].

II. EXPERIMENTAL METHOD

The nanomechanical devices under study are of a simple, doubly clamped beam architecture: 250-nm-thick ribbons, 2–3 μm wide and 100–300 μm long. Their out-of-plane vibrational modes oscillate in the MHz range and exhibit quality factors exceeding 10^5. The resonators are fabricated from stoichiometric silicon nitride grown on a sacrificial silicon dioxide layer on top of a silicon handle. They are patterned using standard optical lithography and reactive ion etching through the nitride and then released using a buffered oxide etch. (A detailed description of the fabrication process is provided in Refs. [26,31,32].) The resulting geometry establishes high tensile strain along the length of the beam; as a consequence, the device acts as a classical string, with its sinusoidal mode shapes [31] enabling the analytical treatments that appear in Sec. III. Molecules are adsorbed onto the nanostrings by vapor deposition of RDX that has been heated and carried to the sample chip via a flow of nitrogen gas. It is observed that the RDX preferentially adsorbs onto the silicon nitride and aggregates in clusters, visible in Fig. 1. We employ various masks to gently bias adsorption around the midpoint of the string. The weak thermal actuation of the string has no effect on where the RDX settles.

Measurements are performed using optical interferometry. Light from a HeNe laser (632.8-nm wavelength) is focused onto the nanostrings, with part of the light reflecting from the surface of the nanostring and part from the silicon substrate underneath the string. The interference of light therefore encodes information on the relative separation between the nanostring and the substrate as a modulation of the optical intensity. The laser power

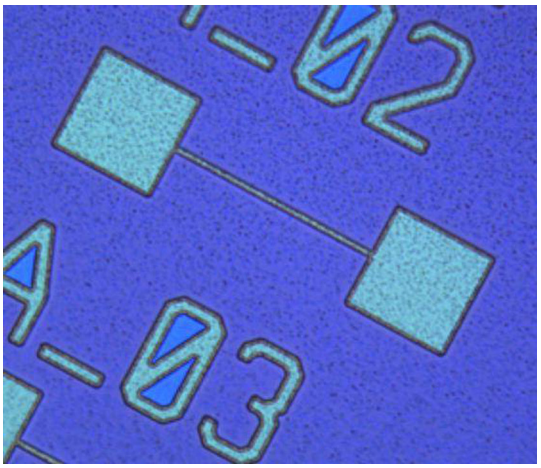

FIG. 1. Optical microscope image showing a 101.7 μm nanostring with a large number of RDX crystallites physisorbed onto the device surface.

incident on the string is no more than 120 μW, and we have shown elsewhere [31] that there is no heating effect.

We focus the laser light halfway along the nanostring. The even-numbered, out-of-plane vibrational modes have a node there, and so our measurements are not sensitive to them [11]. But for the odd-numbered harmonics that we can detect, the string center is always the point of maximum amplitude; hence, we are able to position the laser spot to high accuracy, and the signal-to-noise ratio of the measurement is at its local maximum.

The nanostring chip is placed into an optical-access vacuum chamber, reducing the viscous damping on the resonators [28] and enabling thermomechanical measurements of the nanostrings [11]. The resulting vacuum ($\sim 10^{-4}$ torr) causes sublimation of the RDX from the nanostrings, which is not observed under ambient conditions [35,36]. The HeNe detection laser is not resonant with any of the internal levels of RDX and therefore its light is not adsorbed by the molecule.

A high-frequency Zurich lock-in amplifier (model HF2LI, capable of demodulating as many as six independent frequencies) is used to isolate up to three harmonics that have large thermomechanical displacement at the device midpoint. We track these harmonics as a function of time in order to extract useful information about the distribution of mass on the device surface and about the characteristics of the RDX sublimation process. In practice, the continuous time trace of the optical interferometry measurement $z(t)$ is used to generate a power spectral density (PSD),

$$S(\omega;t) = \frac{1}{T}\int_0^T d\tau\, e^{i\omega\tau}\int_{t-T}^{t-\tau} d\tau'\, z(\tau')z(\tau'+\tau), \quad (1)$$

computed over a sliding time window of duration $T \approx 0.85$ s. The "instantaneous" resonance frequency $\omega_n(t)$ is obtained at each time t by fitting the PSD in the vicinity of its nth peak to the usual (nearly Lorentzian) damped harmonic-oscillator line shape, $S(\omega;t) = A_n\omega_n(t)/\{[\omega_n^2(t)-\omega^2]^2+[\omega\omega_n(t)/Q_n]^2\}$, with the quality factor Q_n and the overall amplitude A_n also optimized as part of the fit [11,31]. This analysis is simple enough that it can be done concurrently with the data acquisition.

III. FRAMEWORK FOR ANALYSIS

A. Frequency shift in response to added mass

We begin by considering the total mechanical energy (kinetic plus potential) of a string of length L vibrating in one of its normal modes,

$$E_n = \int_0^L dx\, \mu(x)\omega_n^2 u_n^2(x). \quad (2)$$

Here, x measures the distance along the string; ω_n and $u_n(x)$ are the angular frequency and displacement profile of mode n; and $\mu(x)$ is the mass per unit length at position x. A small mass perturbation, arising from deposition of a distribution of molecules on the surface of the string, leads to a modified mass distribution $\mu(x) \to \mu(x) + \delta\mu(x)$ and a corresponding frequency shift $\omega_n \to \omega_n + \delta\omega_n$. To leading order, the variations $\delta\mu(x)$ and $\delta\omega_n$ leave the energy stationary ($dE_n = 0$); hence,

$$-2\frac{\delta\omega_n}{\omega_n} = \frac{\int_0^L dx\, \delta\mu(x)u_n^2(x)}{\int_0^L dx\, \mu(x)u_n^2(x)}. \quad (3)$$

Equation (3) can be understood as a linear relationship $\delta\omega_n/\omega_n \propto m/M$ between the relative frequency shift and the ratio of the mass added, $m = \int_0^L dx\, \delta\mu(x)$, to that of the original device, $M = \int_0^L dx\, \mu(x)$. The constant of proportionality

$$-\frac{1}{2}\left(\frac{\int_0^L dx\, \delta\mu(x)u_n^2(x)}{\int_0^L dx\, \delta\mu(x)}\right)\left(\frac{\int_0^L dx\, \mu(x)}{\int_0^L dx\, \mu(x)u_n^2(x)}\right) \quad (4)$$

is unique to each mode and depends on how the resonator's own mass and the mass adsorbed on the surface are arranged.

A variety of other effects can come into play when mass impinges on a resonator [37]. In devices whose vibrational modes are dominated by Young's modulus terms, a molecular covering can induce surface stresses that significantly alter the bending stiffness [38] (which, in the case of cantilevers, can itself be the basis of a detection scheme [39,40]). Additional mass can also provide a new pathway for energy dissipation, so that shifts in the resonant frequencies come about indirectly through changes in the mechanical quality factor. Neither of these effects is relevant to the devices we are studying. Our experiment exploits two properties of nanostrings: (i) they live in a high-tension limit where the bending terms are negligible and the vibrational modes are almost perfectly harmonic, and (ii) they exhibit high mechanical Q that is quite robust to the presence of any molecular overlayer.

For a high-tension string, the mode shape is a sinusoid $u_n(x) = (2/L)^{1/2}\sin(n\pi x/L)$; and, hence,

$$-2\frac{\delta\omega_n}{\omega_n} = \frac{\int_0^L dx\, \delta\mu(x)\sin^2(n\pi x/L)}{\int_0^L dx\, \mu(x)\sin^2(n\pi x/L)}. \quad (5)$$

[The reflection symmetry of u_n^2 imposes the fundamental limitation that $\delta\mu(x)$ cannot be distinguished from $\delta\mu(L-x)$ using frequency-shift measurements alone.] If the unperturbed string has a uniform mass distribution $\mu(x) = M/L$, then Eq. (5) specializes to

$$-\frac{\delta\omega_n}{\omega_n} = \frac{1}{M}\int_0^L dx\, \delta\mu(x)\sin^2\left(\frac{n\pi x}{L}\right). \quad (6)$$

There are two limits worth emphasizing. In the case of a uniform mass deposition profile, with $\delta\mu(x) = m/L$ leading to

$$-\frac{\delta\omega_n}{\omega_n}=\frac{m}{2M}, \tag{7}$$

the mass added m can be determined from a *single* frequency-shift measurement in any mode. A strongly peaked profile represents the extreme opposite case. A point mass m deposited at position x_m leads to

$$-\frac{\delta\omega_n}{\omega_n}=\frac{m}{M}\sin^2\left(\frac{n\pi x_m}{L}\right), \tag{8}$$

and hence the unknown values of m and x_m must be determined from *two* frequency-shift measurements in any pair of modes: specifically,

$$-\frac{m}{M}=\frac{\delta\omega_1}{\omega_1}\left(1-\frac{1}{4}\frac{\delta\omega_2/\omega_2}{\delta\omega_1/\omega_1}\right)^{-1}, \tag{9}$$

$$x_m=\frac{L}{\pi}\arcsin\left(1-\frac{1}{4}\frac{\delta\omega_2/\omega_2}{\delta\omega_1/\omega_1}\right)^{1/2} \tag{10}$$

for modes 1 and 2 (first derived in Ref. [23]); and

$$-\frac{m}{M}=\frac{\delta\omega_1}{\omega_1}\left(\frac{3}{4}\pm\frac{1}{4}\frac{\delta\omega_3/\omega_3}{\delta\omega_1/\omega_1}\right)^{-1}, \tag{11}$$

$$x_m=\frac{L}{\pi}\arcsin\left(\frac{3}{4}\pm\frac{1}{4}\sqrt{\frac{\delta\omega_3/\omega_3}{\delta\omega_1/\omega_1}}\right)^{1/2} \tag{12}$$

for modes 1 and 3.

The general mass-sensing problem, however, is much more difficult than either of these two limits and has the characteristics of an ill-posed inverse problem. The constant of proportionality in the relationship $\delta\omega_n/\omega_n \propto m/M$ is undetermined, and there is no way to recover an arbitrary mass profile $\delta\mu(x)$, except from an infinite number of error-free frequency-shift measurements (or, in practice, from knowledge of $\delta\omega_n/\omega_n$ to sufficient accuracy for all $n = 1, 2, 3, \ldots$ up to a cutoff corresponding to the desired spatial resolution).

We propose to extract the information from the time evolution of the resonance frequencies in a handful of modes by making some reasonable assumptions about $\delta\mu(x)$.

B. Two-parameter mass distribution ansatz

We suggest a simple, two-parameter form to represent the distribution of mass deposited on the string,

$$\delta\mu(x)=\frac{m_0}{L}+\frac{\pi m_1}{2L}\sin\left(\frac{\pi x}{L}\right). \tag{13}$$

Equation (13) is constructed so that m_0 and m_1 have units of mass, and the total mass sitting on the string is

$$\int_0^L dx\,\delta\mu(x)=\frac{m_0}{L}L+\frac{\pi m_1}{2L}\frac{2L}{\pi}=m_0+m_1\equiv m. \tag{14}$$

m_0 is nonnegative, but m_1 may be of either sign. $m_1>0$ describes a convex mass distribution, whereas $-2m_0/\pi < m_1 < 0$ describes a concave one. The lower bound on m_1, which follows from $\delta\mu(L/2)\sim m_0+\pi m_1/2>0$, ensures that the mass distribution remains everywhere nonnegative.

The assumptions behind Eq. (13) are that (i) the distribution is symmetric under reflection about the midpoint of the string and (ii) the distribution is smooth and slowly varying enough that it can be approximated by one component that is uniform across the string and another that places mass preferentially toward (or away from, when $m_1<0$) its center.

Putting Eq. (13) into Eq. (5) gives an expression for the frequency shifts in the various modes,

$$-\frac{\delta\omega_n}{\omega_n}=\frac{1}{M}\left(\frac{m_0}{2}+\frac{2n^2m_1}{4n^2-1}\right). \tag{15}$$

Inverting the relationship, we find that the values of m_0 and m_1 can be estimated from frequency-shift measurements on any pair of modes. For instance, in the case of modes 1 and 2 and modes 1 and 3, we find that

$$\frac{m_0}{M}=8\frac{\delta\omega_1}{\omega_1}-10\frac{\delta\omega_2}{\omega_2},\qquad \frac{m_1}{M}=\frac{15}{2}\left(\frac{\delta\omega_2}{\omega_2}-\frac{\delta\omega_1}{\omega_1}\right); \tag{16}$$

$$\frac{m_0}{M}=\frac{27}{4}\frac{\delta\omega_1}{\omega_1}-\frac{35}{4}\frac{\delta\omega_3}{\omega_3},\qquad \frac{m_1}{M}=\frac{105}{16}\left(\frac{\delta\omega_3}{\omega_3}-\frac{\delta\omega_1}{\omega_1}\right). \tag{17}$$

According to Eq. (15), higher modes (larger n) exhibit decreasing differentiation in the m_1 coefficient and so become less useful for distinguishing the components of the mass distribution, $-\delta\omega_n/\omega_n \to (m_0+m_1)/2M$, independent of n, as $n\to\infty$.

A revealing, preliminary application of this style of analysis is provided in Table I, where Eq. (17) is enlisted to characterize the mass distributed on seven nanostrings of four different lengths following various levels of RDX exposure. In each instance, the resonant frequencies of modes 1 and 3 are measured before and after RDX vapor deposition. We find that the estimates for m_1 exhibit both positive and negative sign (meaning convex and concave mass profiles), and in some cases show magnitude $|m_1|$ comparable to m_0 itself. This is evidence for a quite substantial variation in how RDX settles along the length of the string from one experiment to the next, and it confirms that a mass distribution close to uniform is only rarely the outcome of our sample preparation. The results in Table I are fully consistent with our intentional biasing of the vapor-deposition process.

TABLE I. Results of a sequence of RDX depositions onto nanostrings spanning four different geometries, organized by string length and deposition trial. M is the total predeposition mass inferred from the material density and device volume. Experimentally determined frequency values are reported in columns 5–8, viz., the initial mode frequencies of the first and third harmonics, f_1 and f_3, and the shifts in those frequencies after the mass deposition, δf_1 and δf_3. The ratios m_0/M and m_1/M are obtained from Eq. (17). Traditionally, one would use the shift of the first harmonic alone in conjunction with Eq. (7) to determine the adsorbed mass; we label this quantity m_u, since it is based on the assumption of a uniform mass distribution. Comparison of m_u with the corresponding value $m = m_0 + m_1$, coming from our improved two-component analysis, reveals that the two estimates can differ quite substantially. Fluctuations in the ratio m_u/m indicate that the traditional approach routinely over- or underestimates the adsorbed mass in the range of 10% to 50%. This quantitative comparison demonstrates the absolute importance of a multimode analysis for accurate mass sensing. The dagger (†) marks the one experiment in which the RDX deposition process is completely unbiased; the others involve some degree of masking in order to engineer a nonuniform mass distribution.

Length (μm)	Width (μm)	M (pg)	Trial	f_1 (MHz)	f_3 (MHz)	δf_1 (kHz)	δf_3 (kHz)	m_0/M	m_1/M	$m = m_0 + m_1$ (pg)	m_u (pg)	m_u/m
101.07†	2.83	218.10	1	2.5823	7.7928	−71.083	−210.511	0.0506	0.003 40	11.8	12.0	1.02
172.60	2.05	269.80	1	1.4871	4.4745	−0.100	−0.237	9.56×10^{-6}	93.7×10^{-6}	0.0279	0.0363	1.30
			2	1.4885	4.4785	−1.708	−11.103	0.0139	−0.008 74	1.41	0.619	0.441
			3	1.4898	4.4821	−13.045	−48.873	0.0363	−0.0141	5.99	4.73	0.788
			4	1.4934	4.4931	−2.115	−7.752	0.005 54	−0.002 03	0.947	0.764	0.807
216.34	2.56	422.30	1	1.2104	3.6304	−9.891	−26.318	0.008 27	0.006 05	6.05	6.90	1.14
309.49	2.72	641.88	1	0.8345	2.5067	−2.163	−5.641	0.002 19	0.002 24	2.85	3.33	1.17

How confident should we be in this analysis? One issue that arises is how to quantify the uncertainty arising from our choice of ansatz. The coefficients appearing in Eqs. (16) and (17) are specific to our choice of the sine function in Eq. (13). As a test of the robustness of our assumption, it will be helpful to check the results against an alternative functional form. We therefore also try a symmetric polynomial

$$\delta\mu(x) = m_0 + 6m_1\frac{x}{L}\left(1 - \frac{x}{L}\right). \tag{18}$$

It is also important to look for consistency between the results achieved with measurements on different sets of modes. As discussed in Sec. II, the laser in our optical detection system is parked at the string midpoint, so only the odd-numbered modes are measured. Table II lists all the possible mass determinations using frequency shifts in modes 1, 3, and 5 (exact determinations with the three available pairs and one overdetermination with the full triplet of modes), under the assumption of a mass profile following either Eq. (13) or Eq. (18).

A reasonable final value of the fractional mass added comes from averaging those eight estimates,

$$\frac{m}{M} = \frac{m_0 + m_1}{M} = 0.108\,031\frac{\delta\omega_1}{\omega_1} - 0.534\,596\frac{\delta\omega_3}{\omega_3} - 1.573\,434\frac{\delta\omega_5}{\omega_5}. \tag{19}$$

The total uncertainty, $(\Delta_e[m/M]^2 + \Delta_a[m/M]^2)^{1/2}$, is taken to be a combination of the experimental errors arising from imperfect knowledge of the relative frequency shifts,

TABLE II. Estimates of the uniform (m_0) and nonuniform (m_1) mass components as a function of the relative frequency shifts. A solution to the system of equations is given for each pair of modes; also shown is the least-squares, pseudoinverse solution involving all three modes.

Ansatz	Modes	m_0/M	m_1/M
Eq. (13)	1, 3	$\frac{27}{4}\frac{\delta\omega_1}{\omega_1} - \frac{35}{4}\frac{\delta\omega_3}{\omega_3}$	$\frac{105}{16}\left(-\frac{\delta\omega_1}{\omega_1} + \frac{\delta\omega_3}{\omega_3}\right)$
	1, 5	$\frac{25}{4}\frac{\delta\omega_1}{\omega_1} - \frac{33}{4}\frac{\delta\omega_5}{\omega_5}$	$\frac{99}{16}\left(-\frac{\delta\omega_1}{\omega_1} + \frac{\delta\omega_5}{\omega_5}\right)$
	3, 5	$\frac{875}{8}\frac{\delta\omega_3}{\omega_3} - \frac{891}{8}\frac{\delta\omega_5}{\omega_5}$	$\frac{3465}{32}\left(-\frac{\delta\omega_3}{\omega_3} + \frac{\delta\omega_5}{\omega_5}\right)$
	1, 3, 5	$\frac{15\,007}{2318}\frac{\delta\omega_1}{\omega_1} - \frac{36\,365}{37\,088}\frac{\delta\omega_3}{\omega_3} - \frac{128\,205}{37\,088}\frac{\delta\omega_5}{\omega_5}$	$-\frac{58\,905}{9272}\frac{\delta\omega_1}{\omega_1} + \frac{107\,415}{9272}\frac{\delta\omega_3}{\omega_3} + \frac{42\,207}{9272}\frac{\delta\omega_5}{\omega_5}$
Eq. (18)	1, 3	$\frac{1+3\pi^2}{4}\frac{\delta\omega_1}{\omega_1} - \frac{9+3\pi^2}{4}\frac{\delta\omega_3}{\omega_3}$	$\frac{3\pi^2}{4}\left(-\frac{\delta\omega_1}{\omega_1} + \frac{\delta\omega_3}{\omega_3}\right)$
	1, 5	$\frac{3+25\pi^2}{36}\frac{\delta\omega_1}{\omega_1} - \frac{25(3+\pi^2)}{36}\frac{\delta\omega_5}{\omega_5}$	$\frac{25\pi^2}{36}\left(-\frac{\delta\omega_1}{\omega_1} + \frac{\delta\omega_5}{\omega_5}\right)$
	3, 5	$\frac{9+75\pi^2}{8}\frac{\delta\omega_3}{\omega_3} - \frac{25(1+3\pi^2)}{8}\frac{\delta\omega_5}{\omega_5}$	$-\frac{75\pi^2}{8}\left(-\frac{\delta\omega_3}{\omega_3} + \frac{\delta\omega_5}{\omega_5}\right)$
	1, 3, 5	$\frac{217+975\pi^2}{1358}\frac{\delta\omega_1}{\omega_1} - \frac{5607+1725\pi^2}{5432}\frac{\delta\omega_3}{\omega_3} - \frac{6125+2175\pi^2}{5432}\frac{\delta\omega_5}{\omega_5}$	$\frac{75\pi^2}{5432}\left(-\frac{52\delta\omega_1}{\omega_1} + \frac{23\delta\omega_3}{\omega_3} + \frac{29\delta\omega_5}{\omega_5}\right)$

$$\Delta_e\left[\frac{m}{M}\right]^2 = 0.0117\Delta_e\left[\frac{\delta\omega_1}{\omega_1}\right]^2 + 0.2858\Delta_e\left[\frac{\delta\omega_3}{\omega_3}\right]^2 + 2.4757\Delta_e\left[\frac{\delta\omega_5}{\omega_5}\right]^2, \quad (20)$$

and the uncertainty due to the choice of ansatz, which we approximate by the spread around the mean estimate given in Eq. (19),

$$\Delta_a\left[\frac{m}{M}\right]^2 = 0.007\,91\left(\frac{\delta\omega_1}{\omega_1}\right)^2 + 1.7344\left(\frac{\delta\omega_3}{\omega_3}\right)^2 + 1.5138\left(\frac{\delta\omega_5}{\omega_5}\right)^2 - 0.2285\frac{\delta\omega_1}{\omega_1}\frac{\delta\omega_3}{\omega_3} + 0.2127\frac{\delta\omega_1}{\omega_1}\frac{\delta\omega_5}{\omega_5} - 3.2403\frac{\delta\omega_3}{\omega_3}\frac{\delta\omega_5}{\omega_5}. \quad (21)$$

The notation $\Delta_e[\delta\omega_n/\omega_n]$ in Eq. (20) is meant to indicate the error in the relative frequency shift, understood as the ratio of two inexact quantities computed according to $\Delta_e[\delta\omega_n/\omega_n]^2 = (\Delta_e[\delta\omega_n]/\omega_n)^2 + (\Delta_e[\omega_n]\delta\omega_n/\omega_n^2)^2$.

C. Sublimation model

The preliminary results appearing in Table I are obtained from two discrete measurements of the devices' resonance frequencies, before and after RDX exposure. We have the capability, however, to make ongoing measurements of the resonance frequencies; these change continuously in time as the adsorbate molecules are removed from the nanostring because of the vacuum environment. The main thrust of this paper is to show how we can exploit this much richer data set.

Therefore it is useful to sketch out a model of how the mass on the string evolves with time in our experimental setup. The basic assumption is that the molecules are either residing on the string (m) or existing as vapor in the chamber (m_v). RDX sublimates from the string surface at a uniform rate α, and there is an incoming flux of molecules returning to the surface due to intermolecular collisions, denoted by β. Finally, there is γ, the rate at which the chamber is being evacuated. This picture leads to a coupled pair of rate equations,

$$\frac{d}{dt}\begin{pmatrix} m \\ m_v \end{pmatrix} = \begin{pmatrix} -\alpha & \beta \\ \alpha & -(\beta+\gamma) \end{pmatrix}\begin{pmatrix} m \\ m_v \end{pmatrix}. \quad (22)$$

As a consequence, there are two rate constants, given by the eigenvalues of the matrix. When $\gamma = 0$, the eigenvalues are $\lambda_1 = 0$ and $\lambda_2 = \alpha + \beta$; hence, the system equilibrates at a rate $\alpha + \beta$ to a steady state with $m_v/m = \alpha/\beta$. On the other hand, when γ is a fast rate (i.e., larger than both α and β, which is the experimentally relevant situation), we find that

$$\lambda_1 = -\alpha + \frac{\alpha\beta}{\gamma} + \frac{\alpha\beta(\alpha-\beta)}{\gamma^2} + O(\gamma^{-3}),$$
$$\lambda_2 = -\gamma - \beta - \frac{\alpha\beta}{\gamma} - \frac{\alpha\beta(\alpha-\beta)}{\gamma^2} + O(\gamma^{-3}). \quad (23)$$

The full time dependence of m and m_v is then given by

$$\begin{pmatrix} m(t) \\ m_v(t) \end{pmatrix} = \frac{\gamma m(0) + \beta m_v(0)}{\gamma^2 + \alpha\beta}\begin{pmatrix} \gamma \\ \alpha \end{pmatrix} e^{-(\alpha - \alpha\beta/\gamma)t} + \frac{\gamma m_v(0) - \alpha m(0)}{\gamma^2 + \alpha\beta}\begin{pmatrix} -\beta \\ \gamma \end{pmatrix} e^{-(\gamma+\beta+\alpha\beta/\gamma)t}. \quad (24)$$

For times $t \gg (\gamma + \beta + \alpha\beta/\gamma)^{-1}$, the mass on the string decays according to

$$m(t) = \frac{m(0) + (\beta/\gamma)m_v(0)}{1 + \alpha\beta/\gamma^2} e^{-\alpha(1-\beta/\gamma)t}. \quad (25)$$

Moreover, if the chamber is being very aggressively evacuated, then the behavior looks like

$$m(t) = m(0)e^{-\alpha_{\text{eff}}t}, \quad (26)$$

with $\alpha_{\text{eff}} = \alpha - \alpha\beta/\gamma \approx \alpha$ close to the intrinsic sublimation rate of the adsorbate, and we can safely proceed as if $m_v \approx 0$ at all times after the pump is activated.

A refinement of this model is to consider the possibility that the rate of mass loss goes as a fractional power of the current mass load. This may be appropriate here since the RDX on the surface is known to aggregate, rather than arranging in a smooth monolayer. Sublimation in that case is likely to be at least partially controlled by loss from the surface area of the RDX crystallites ($A \sim m^{2/3}$), which puts a lower bound of $2/3$ on the effective scaling exponent. If the distribution of crystallites along the device is roughly uniform, then we can account for this situation as follows:

$$\frac{dm}{dt} = -\alpha m_\star (m/m_\star)^\phi. \quad (27)$$

This description requires that we introduce a new material-specific mass scale $m_\star$ and a phenomenological exponent ϕ. We anticipate a value $2/3 \le \phi \le 1$, with conventional exponential decay recovered at the upper end of that range. When $\phi \neq 1$, we find that

$$\frac{dm}{m^\phi} = \frac{1}{1-\phi}d(m^{1-\phi}) = -\alpha m_\star^{1-\phi}dt.$$

This leads to

$$m(t) = m(0)\left[1 - \frac{t}{t_r}\right]^{1/(1-\phi)}, \quad (28)$$

where, $t_r = [m(0)/m_\star]^{1-\phi}/\alpha(1-\phi)$ is the finite removal time after which all RDX has left the nanostring.

We now emphasize an important feature that distinguishes between the two kinds of behavior. When $\phi = 1$, the decay is exponential at a constant rate

$$-\frac{1}{t}\ln\frac{m(t)}{m(0)} = \alpha. \tag{29}$$

For a nontrivial value of the exponent, however, the mass loss is characterized by an apparent decay rate that increases over time,

$$\begin{aligned}
&-\frac{1}{t}\ln\frac{m(t)}{m(0)} \\
&= -\frac{1}{(1-\phi)t}\ln\left[1-\frac{t}{t_r}\right] \\
&= \frac{1}{(1-\phi)t_r}\left[1+\frac{t}{2t_r}+\frac{t^2}{3t_r^2}+\cdots\right] \\
&= \alpha\left(\frac{m_\star}{m(0)}\right)^{1-\phi}\left[1+\frac{(1-\phi)\alpha t}{2}\left(\frac{m_\star}{m(0)}\right)^{1-\phi}+\cdots\right].
\end{aligned} \tag{30}$$

Finally, a more complete description must account for a mass distribution that varies along the length of the string. We treat the deposited mass $\delta\mu(x,t)$ as a space- and time-dependent field subject to the governing equation

$$\frac{\partial}{\partial t}\delta\mu(x,t) = -\alpha\mu_\star\left(\frac{\delta\mu(x,t)}{\mu_\star}\right)^{\phi}. \tag{31}$$

Here, $\mu_\star$ is a stand-in for $m_\star/L$. In the previously considered situations, where either $\phi = 1$ or the initial mass distribution is uniform, the mass distribution simply shrinks away while preserving its overall shape. That is not generally true,

$$\delta\mu(x,t) = [\delta\mu(x,0)^{1-\phi} - (1-\phi)\alpha\mu_\star^{1-\phi}t]^{1/(1-\phi)}. \tag{32}$$

Equation (32) also makes clear that, unlike in Eq. (28), $\delta\mu$ reaches zero at a removal time that is different at each point along the string.

With Eq. (32) in hand, it is straightforward to obtain the time-dependent total mass

$$m(t) = \int_0^L dx\,\delta\mu(x,t) \tag{33}$$

or any of the relative frequency shifts

$$-\frac{\delta\omega_n(t)}{\omega_n} = \frac{1}{M}\int_0^L dx\delta\mu(x,t)\sin^2\left(\frac{n\pi x}{L}\right). \tag{34}$$

The latter is simply Eq. (6) with $\delta\mu(x)$ replaced by $\delta\mu(x,t)$.

IV. RESULTS

We now apply the models developed in Sec. III to our experimentally acquired frequency shifts. The results reported here are taken from measurements on a single device of length 310 μm and mass 641.88 pg. The device's first, third, and fifth modes are tracked over the course of 4 h.

Our approach is to match Eq. (34), for the cases of $n = 1, 3, 5$, to our time traces of the resonance frequencies. The integrals are carried out numerically with Eq. (32) serving as the model for $\delta\mu(x,t)$. In the spirit of our original two-component ansatz, we choose to express the initial mass distribution in this slightly more expressive form,

$$\delta\mu(x,0) = \frac{m_0}{L} + \frac{m_1}{L}N(p)\left[\frac{x}{L}\left(1-\frac{x}{L}\right)\right]^p. \tag{35}$$

The exponent p adds some additional flexibility with regard to the shape of the nonuniform contribution [and permits a rough interpolation between Eqs. (13) and (18)]. The normalization factor

$$N(p) = \frac{2^{1+2\theta}}{\sqrt{\pi}}\frac{\Gamma(3/2+p)}{\Gamma(1+p)}$$

is chosen to preserve the property that $m = \int dx\,\delta\mu(x,0) = m_0 + m_1$.

The set of independent variational parameters m_0, m_1, p, ϕ, and $C = (1-\phi)\alpha\mu_\star^{1-\phi}$ is simultaneously optimized using the nonlinear least-squares Levenberg-Marquardt algorithm [41,42]. The number of degrees of freedom—only five—is remarkably small relative to the large number ($\approx 3 \times 7000$) of data points. We find that the total mass on the string is $m_0 + m_1 = 2.871(2)$ pg and that the decay exponent has a value $\phi = 0.826(6)$. The resulting high-quality fit is displayed in the upper panel of Fig. 2. The lower panel of the same figure shows the mass extracted at each instant from frequency-shift measurements according to Eq. (19), with error bars on the data points obtained from the quadratic mean of Eqs. (20) and (21). There are a handful of points in the plot where the uncertainty estimate blows up, but this amounts to just a few blips in the more than 7000 data points. The solid line superimposed on the data points is produced by integrating [via Eq. (33)] the evolving mass profile that emerges from the fitting procedure [Eq. (32), with globally optimized parameters]. The consistency between these two approaches gives us confidence that our estimate of the total adsorbed mass is highly reliable.

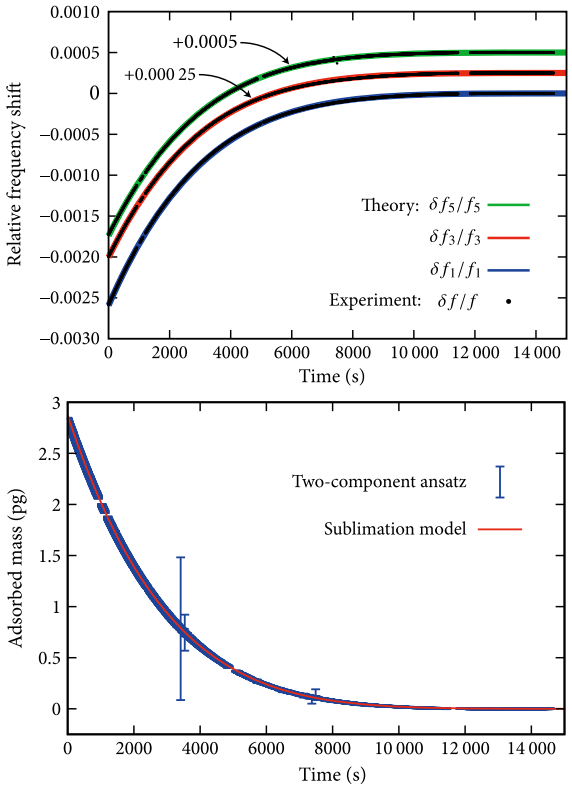

FIG. 2. Multimode frequency shifts as a function of elapsed time and the resulting RDX mass extraction. In the upper panel, each experimental data point represents a relative shift in the resonance frequency of one of modes 1, 3, or 5, obtained from the finite-time-window PSD [as per Eq. (1)]. (The time-window resolution is fine enough that the experimental points bleed together into nearly continuous curves.) For visual clarity, the mode 3 and mode 5 data sets are translated upward by 0.000 25 and 0.0005, respectively. The three solid lines are the result of matching our theoretical model [viz., Eq. (34) in combination with Eqs. (32) and (35)] to the experimental observations. The lower panel shows the corresponding mass. Two estimates are presented: one is a discrete set of values calculated at each instant according to Eqs. (19)–(21); the other is a continuous curve [produced numerically with Eq. (33)] based on the global fit achieved in the upper panel. The two estimates are found to be in excellent agreement.

Figure 3 shows snapshots of the mass profile at various times in the experiment. Such a determination of the real-time mass distribution may have important applications, such as the study of diffusion of molecules along the surface [43], or atomic layer reconstruction [44], of a nanomechanical resonator.

Figure 4 indicates the effective instantaneous decay rate, calculated as per Eqs. (29) and (30). One can see clearly that the rate is not constant in time—and hence it is incompatible with pure exponential decay. Rather, it seems to increase steadily. Moreover, between 8000 s and 11 000 s, it turns up in a way that is consistent with the fractional power of ϕ found in our fit to the

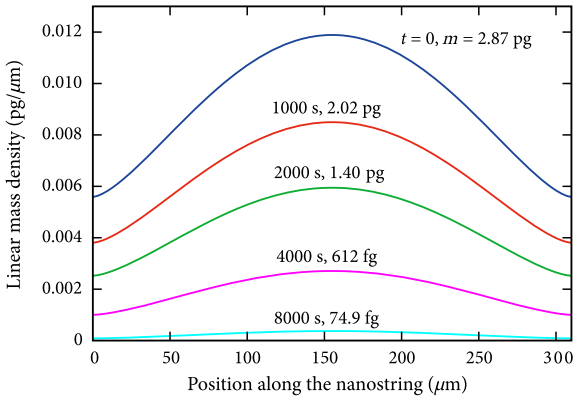

FIG. 3. Profiles of the mass distributed along the nanostring of length 310 μm and mass 641.88 pg at representative moments in time. Shown here are plots of Eq. (32) evaluated with optimized variational parameters at the appropriate time t. Accompanying each distribution is a label giving the time of the snapshot and integrated weight under the curve.

frequency-shift measurements. It is worth reiterating that this implies that sublimation occurs from the surface of crystallites—and not uniformly from the surface of the device—in agreement with optical (see Fig. 1) and atomic force (see Ref. [34]) microscopy.

Something further we have checked is whether the fitting can be meaningfully improved by allowing $\alpha \to \alpha(x)$ to vary along the length of the string. One might imagine, for instance, that the sublimation rate has a uniform contribution controlled by the partial pressure of RDX in the evacuated chamber and a locally varying component that comes about in some unspecified way from the influence of the mechanical motion. We have carefully considered various *ad hoc* models, but we find consistently that allowing spatial

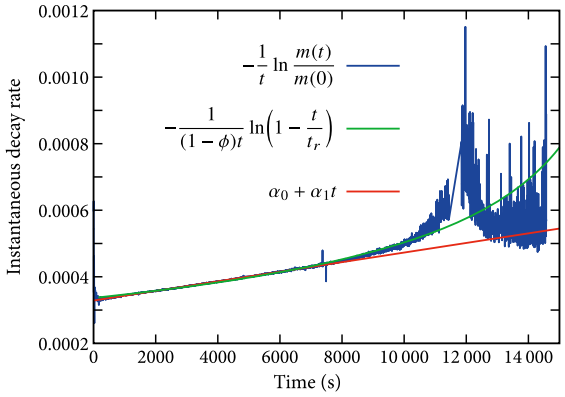

FIG. 4. The instantaneous rate at which RDX desorbs from the nanostring clearly increases over time. The data shown are a logarithmic rescaling of the data appearing in the lower panel of Fig. 2. A linear fit over the time interval [250 s, 7750 s] produces $\alpha(t) = \alpha_0 + \alpha_1 t = 0.000\,328\,65(6) + 1.445(1) \times t$. Substantially better agreement is achieved with a function having the form of Eq. (30) with exponent $\phi = 0.8278$ [fully consistent with the value $\phi = 0.826(6)$ used in the upper panel of Fig. 2] and removal time $t_r = 17\,247$ s.

variation in $\alpha(x)$ does not improve the fit enough to justify the additional variational degrees of freedom [45].

V. CONCLUSIONS

Taking advantage of the sinusoidal mode shape of silicon nitride nanostrings under high tension, we develop analytical models for the multimode frequency shifts that occur as a result of mass deposited onto such devices. We apply those models to real resonators in the lab and demonstrate our ability to make reliable estimates of the total amount and distribution of adsorbed molecules. This work provides experimental determination of a mass distribution that is neither uniform nor pointlike.

Our multimode technique produces reliable, time-evolving estimates of the total mass adsorbed on the resonator with a sensitivity on the order of a few femtograms, even in the absence of detailed knowledge of the initial mass distribution. The time trace of frequency measurements in a handful of low-lying normal modes is sufficient to reconstruct that missing information and thus fix the otherwise unknown constant of proportionality [appearing as Eq. (4)].

Notably, the estimate of the mass added, as determined by our analysis, is often found to disagree with the value arrived at by the more traditional approach, which relies on a frequency shift in a single mode and incorporates no understanding of how the added mass is arranged on the device. This reveals the extreme importance of such an analysis to accurate mass sensing with nanomechanical resonators.

In addition, because the adsorbed molecules sublimate from the surface of the nanostrings in our experimental system, we have had an opportunity to analyze their desorption characteristics. Real-time measurements allow for significantly improved estimates of the mass distributions and reveal the evolution of those distributions over time. This may prove a useful tool in studying molecular diffusion [43] or the formation of monolayers on nanomechanical resonators [44].

Finally, multimode analysis also leads to insights into the manner in which the molecules are removed from the nanostring surface by the vacuum. Specifically, we are able to develop sublimation models that account for uniform-rate loss from the surface and local-mass-dependent loss from the surface area of a crystallite. Only the latter is consistent with the observed frequency shifts and the microscopy of the devices. This may have important applications in real-world sensing of explosive molecules such as RDX, for example, in airport-passenger and luggage screening.

ACKNOWLEDGMENTS

The authors acknowledge support from the Natural Sciences and Engineering Research Council of Canada; the Canada Foundation for Innovation; Alberta Innovates Technology Futures; Grand Challenges Canada; Alberta Innovates Health Solutions; and the Office of Research and Sponsored Programs of the University of Mississippi. One of the authors (K. S. D. B.) benefitted from a stay at the Aspen Center for Physics under NSF Grant No. 1066293.

[1] G. Y. Chen, T. Thundat, E. A. Wachter, and R. J. Warmack, Adsorption-induced surface stress and its effects on resonance frequency of microcantilevers, J. Appl. Phys. **77**, 3618 (1995).

[2] T. Thundat, E. A. Wachter, S. L. Sharp, and R. J. Warmack, Detection of mercury-vapor using resonating microcantilevers, Appl. Phys. Lett. **66**, 1695 (1995).

[3] J. L. Arlett, E. B. Myers, and M. L. Roukes, Comparative advantages of mechanical biosensors, Nat. Nanotechnol. **6**, 203 (2011).

[4] Y. T. Yang, C. Callegari, X. L. Feng, K. L. Ekinci, and M. L. Roukes, Zeptogram-scale nanomechanical mass sensing, Nano Lett. **6**, 583 (2006).

[5] K. Jensen, K. Kim, and A. Zettl, An atomic-resolution nanomechanical mass sensor, Nat. Nanotechnol. **3**, 533 (2008).

[6] J. Chaste, A. Eichler, J. Moser, G. Ceballos, R. Rurali, and A. Bachtold, A nanomechanical mass sensor with yoctogram resolution, Nat. Nanotechnol. **7**, 301 (2012).

[7] S. Olcum *et al.*, Weighing nanoparticles in solution at the attogram scale, Proc. Natl. Acad. Sci. U.S.A. **111**, 1310 (2014).

[8] K. L. Ekinci, X. M. H. Huang, and M. L. Roukes, Ultrasensitive nanoelectromechanical mass detection, Appl. Phys. Lett. **84**, 4469 (2004).

[9] B. Ilic, Y. Yang, and H. G. Craighead, Virus detection using nanoelectromechanical devices, Appl. Phys. Lett. **85**, 2604 (2004).

[10] B. Ilic, H. G. Craighead, S. Krylov, W. Senaratne, C. Ober, and P. Neuzil, Attogram detection using nanoelectromechanical oscillators, J. Appl. Phys. **95**, 3694 (2004).

[11] B. D. Hauer, C. Doolin, K. S. D. Beach, and J. P. Davis, A general procedure for thermomechanical calibration of nano/micro-mechanical resonators, Ann. Phys. (N.Y.) **339**, 181 (2013).

[12] A. K. Naik, M. S. Hanay, W. K. Hiebert, X. L. Feng, and M. L. Roukes, Towards single-molecule nanomechanical mass spectrometry, Nat. Nanotechnol. **4**, 445 (2009).

[13] V. T. K. Sauer, M. R. Freeman, and W. K. Hiebert, Device overshield for mass sensing enhancement (DOME) structure fabrication, J. Micromech. Microeng. **20**, 105020 (2010).

[14] M. S. Hanay, S. Kelber, A. K. Naik, D. Chi, S. Hentz, E. C. Bullard, E. Colinet, L. Duraffourg, and M. L. Roukes, Single-protein nanomechanical mass spectrometry in real time, Nat. Nanotechnol. **7**, 602 (2012).

[15] J. Lee, A. K. Bryan, and S. R. Manalis, High precision particle mass sensing using microchannel resonators in the second vibration mode, Rev. Sci. Instrum. **82**, 023704 (2011).

[16] J. D. Parkin and G Hähner, Mass determination and sensitivity based on resonance frequency changes of the higher

flexural modes of cantilever sensors, Rev. Sci. Instrum. **82**, 035108 (2011).
[17] D. Kim, S. Hong, J. Jang, and J. Park, Simultaneous determination of position and mass in the cantilever sensor using transfer function method, Appl. Phys. Lett. **103**, 033108 (2013).
[18] R. Perenon, E. Sage, A. Mohammad-Djafari, L. Duraffourg, S. Hentz, A. Brenac, R. Morel, and P. Grangeat, in *Proceedings of the 21st European Signal Processing Conference, Marrakesh, 2013* (IEEE, New York, 2013).
[19] Z. Wang, J. Lee, and P. X.-L. Feng, Spatial mapping of multimode Brownian motions in high-frequency silicon carbide microdisk resonators, Nat. Commun. **5**, 5158 (2014).
[20] M. Selim Hanay, Scott I. Kelber, Cathal D. O'Connell, Paul Mulvaney, John E. Sader, and Michael L. Roukes, Inertial imaging with nanomechanical systems, Nat. Nanotechnol. **10**, 339 (2015).
[21] W. H. Press, S. A. Teukolsky, W. T. Vetterling, and B. P. Flannery, in *Numerical Recipes: The Art of Scientific Computing*, 3rd ed. (Cambridge University Press, New York, 2007).
[22] S. Dohn, W. Svendsen, A. Boisen, and O. Hansen, Mass and position determination of attached particles on cantilever based mass sensors, Rev. Sci. Instrum. **78**, 103303 (2007).
[23] S. Schmid, S. Dohn, and A. Boisen, Real-time particle mass spectrometry based on resonant micro strings, Sensors **10**, 8092 (2010).
[24] I. Stachiv, A. I. Fedorchenko, and Y.-L. Chen, Mass detection by means of the vibrating nanomechanical resonators, Appl. Phys. Lett. **100**, 093110 (2012).
[25] Yin Zhang and Yun Liu, Detecting both the mass and position of an accreted particle by a micro/nano-mechanical resonator sensor, Sensors **14**, 16296 (2014).
[26] T. S. Biswas, Jin Xu, X. Rojas, C. Doolin, A. Suhel, K. S. D. Beach, and J. P. Davis, Remote sensing in hybridized arrays of nanostrings, Nano Lett. **14**, 2541 (2014).
[27] S. S. Verbridge, J. M. Parpia, R. B. Reichenbach, L. M. Bellan, and H. G. Craighead, High quality factor resonance at room temperature with nanostrings under high tensile stress, J. Appl. Phys. **99**, 124304 (2006).
[28] S. S. Verbridge, H. G. Craighead, and J. M. Parpia, A megahertz nanomechanical resonator with room temperature quality factor over a million, Appl. Phys. Lett. **92**, 013112 (2008).
[29] X. Feng, R. He, P. Yang, and M. Roukes, Very high frequency silicon nanowire electromechanical resonators, Nano Lett. **7**, 1953 (2007).
[30] S. Schmid, K. D. Jensen, K. H. Nielsen, and A. Boisen, Damping mechanisms in high-Q micro and nanomechanical string resonators, Phys. Rev. B **84**, 165307 (2011).
[31] A. Suhel, B. D. Hauer, T. S. Biswas, K. S. D. Beach, and J. P. Davis, Dissipation mechanisms in thermomechanically driven silicon ntride nanostrings, Appl. Phys. Lett. **100**, 173111 (2012).
[32] T. S. Biswas, A. Suhel, B. D. Hauer, A. Palomino, K. S. D. Beach, and J. P. Davis, High-Q gold and silicon nitride bilayer nanostrings, Appl. Phys. Lett. **101**, 093105 (2012).
[33] M. J. Seitner, K. Gajo, and E. M. Weig, Damping of metallized bilayer nanomechanical resonators at room temperature, Appl. Phys. Lett. **105**, 213101 (2014).
[34] T. S. Biswas, N. Miriyala, C. Doolin, X. Liu, T. Thundat, and J. P. Davis, Femtogram-scale photothermal spectroscopy of explosive molecules on nanostrings, Anal. Chem. **86**, 11368 (2014).
[35] G. Muralidharana, A. Wig, L. A. Pinnaduwage, D. Hedden, T. Thundat, and Richard T. Lareau, Adsorption-desorption characteristics of explosive vapors investigated with microcantilevers, Ultramicroscopy **97**, 433 (2003).
[36] L. A. Pinnaduwage, T. Thundat, A. Gehla, S. D. Wilson, D. L. Hedden, and R. T. Lareau, Desorption characteristics of uncoated silicon micro cantilever surfaces for explosive and common nonexplosive vapors, Ultramicroscopy **100**, 211 (2004).
[37] Yin Zhang, Determining the adsorption-induced surface stress and mass by measuring the shifts of resonant frequencies, Sens. Actuators, A **194**, 169 (2013).
[38] D. W. Dareing and T. Thundat, Simulation of adsorption-induced stress of a microcantilever sensor, J. Appl. Phys. **97**, 043526 (2005).
[39] R. Berger, E. Delamarche, H. P. Lang, C. Gerber, J. K. Gimzewski, E. Meyer, and H.-J. Güntherodt, Surface stress in the self-assembly of alkanethiols on gold, Science **276**, 2021 (1997).
[40] H. P. Lang, M. Hegner, E. Meyer, and Ch. Gerber, Nanomechanics from atomic resolution to molecular recognition based on atomic force microscopy technology, Nanotechnology **13**, R29 (2002).
[41] K. Levenberg, A method for the solution of certain nonlinear problems in least squares, Q. Appl. Math. **2**, 164 (1944).
[42] D. W. Marquardt, An algorithm for least-squares estimation of nonlinear parameters, J. Soc. Ind. Appl. Math. **11**, 431 (1963).
[43] Y. T. Yang, C. Callegari, X. L. Feng, and M. L. Roukes, Surface adsorbate fluctuations and noise in nanoelectromechanical systems, Nano Lett. **11**, 1753 (2011).
[44] A. Tavernarakis, J. Chaste, A. Eichler, G. Ceballos, M. C. Gordillo, J. Boronat, and A. Bachtold, Atomic Monolayer Deposition on the Surface of Nanotube Mechanical Resonators, Phys. Rev. Lett. **112**, 196103 (2014).
[45] H. Akaike, A new look at the statistical model identification, IEEE Trans. Autom. Control **19**, 716 (1974).